Landslide mobility and hazards: implications of the 2014 Oso disaster

R.M. Iverson [a,*], D.L. George [a], K. Allstadt [b,1], M.E. Reid [c], B.D. Collins [c], J.W. Vallance [a], S.P. Schilling [a], J.W. Godt [d], C.M. Cannon [e], C.S. Magirl [f], R.L. Baum [d], J.A. Coe [d], W.H. Schulz [d], J.B. Bower [g]

[a] U.S. Geological Survey, Vancouver, WA, USA
[b] University of Washington, Seattle, WA, USA
[c] U.S. Geological Survey, Menlo Park, CA, USA
[d] U.S. Geological Survey, Denver, CO, USA
[e] U.S. Geological Survey, Portland, OR, USA
[f] U.S. Geological Survey, Tacoma, WA, USA
[g] NOAA National Weather Service, Seattle, WA, USA

A B S T R A C T

Landslides reflect landscape instability that evolves over meteorological and geological timescales, and they also pose threats to people, property, and the environment. The severity of these threats depends largely on landslide speed and travel distance, which are collectively described as landslide "mobility". To investigate causes and effects of mobility, we focus on a disastrous landslide that occurred on 22 March 2014 near Oso, Washington, USA, following a long period of abnormally wet weather. The landslide's impacts were severe because its mobility exceeded that of prior historical landslides at the site, and also exceeded that of comparable landslides elsewhere. The $\sim 8 \times 10^6$ m^3 landslide originated on a gently sloping ($<20°$) riverside bluff only 180 m high, yet it traveled across the entire ~ 1 km breadth of the adjacent floodplain and spread laterally a similar distance. Seismological evidence indicates that high-speed, flowing motion of the landslide began after about 50 s of preliminary slope movement, and observational evidence supports the hypothesis that the high mobility of the landslide resulted from liquefaction of water-saturated sediment at its base. Numerical simulation of the event using a newly developed model indicates that liquefaction and high mobility can be attributed to compression- and/or shear-induced sediment contraction that was strongly dependent on initial conditions. An alternative numerical simulation indicates that the landslide would have been far less mobile if its initial porosity and water content had been only slightly lower. Sensitive dependence of landslide mobility on initial conditions has broad implications for assessment of landslide hazards.

Published by Elsevier B.V. This is an open access article under the CC BY-NC-ND license (http://creativecommons.org/licenses/by-nc-nd/4.0/).

1. Introduction

Landslide mobility has long intrigued earth and planetary scientists (Legros, 2002). The vexing nature and practical significance of the phenomenon were first recognized in 1881, when much of the town of Elm, Switzerland, was buried by a landslide involving about 10^7 m^3 of material that traversed a path 2017 m in length (L) as it descended from a maximum height (H) of 613 m (Hsu, 1978). The Elm disaster motivated development of a landslide mobility index known as the fahrböschung (Heim, 1882, 1932), or more commonly, as the H/L ratio (Corominas, 1996). The Elm landslide had $H/L \approx 0.3$, and $H/L < 0.6$ was once thought to be indicative of anomalously low intrinsic friction exhibited by many landslides with volumes greater than about 10^6 m^3 (Scheidegger, 1973). Recent field, laboratory and theoretical investigations have largely discredited this notion, in part because H/L is an inadequate measure of bulk frictional resistance (e.g., Corominas, 1996; Iverson, 1997; Dade and Huppert, 1998; Legros, 2002; Iverson et al., 2011; Farin et al., 2014). Nevertheless, H/L values (or their reciprocals, L/H values) serve an important practical purpose be-

* Corresponding author at: U.S. Geological Survey, 1300 SE Cardinal Ct., Vancouver, WA 98683, United States. Tel.: +1 360 993 8920; fax: +1 360 993 8980.
E-mail addresses: riverson@usgs.gov (R.M. Iverson), dgeorge@usgs.gov (D.L. George), kallstadt@usgs.gov (K. Allstadt), mreid@usgs.gov (M.E. Reid), bcollins@usgs.gov (B.D. Collins), vallance@usgs.gov (J.W. Vallance), sschilli@usgs.gov (S.P. Schilling), jgodt@usgs.gov (J.W. Godt), ccannon@usgs.gov (C.M. Cannon), magirl@usgs.gov (C.S. Magirl), baum@usgs.gov (R.L. Baum), jcoe@usgs.gov (J.A. Coe), wschulz@usgs.gov (W.H. Schulz), brent.bower@noaa.gov (J.B. Bower).
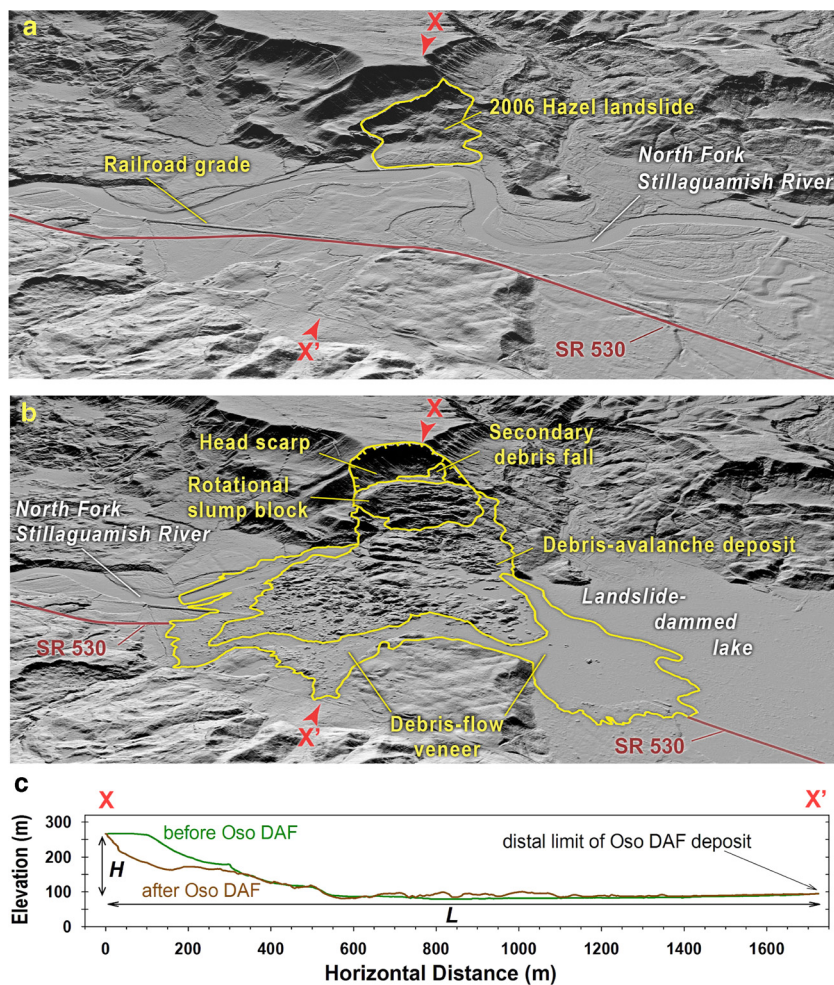[1] Current address: U.S. Geological Survey, Vancouver, Washington, USA.

Fig. 1. Shaded relief lidar images and longitudinal topographic profiles of the Oso DAF site. a and b: Northwest-looking oblique perspectives of major geomorphic and cultural features visible in 2013 and 2014 lidar imagery acquired before and after the Oso DAF occurred. The DAF encompasses the entire area enclosed by the outer yellow line in b. c: Longitudinal topographic profiles and definitions of H and L along the transect $X - X'$ shown in a and b. (For interpretation of the references to color in this figure legend, the reader is referred to the web version of this article.)

cause they identify locations that can be overrun by a landslide with a specific source area and sufficiently large L/H value.

A landslide near Oso, Washington, USA, on 22 March 2014 had a volume of about 8×10^6 m^3, similar to that of the Elm landslide of 1881, but its mobility (as gauged by $H/L = 0.105$ or $L/H = 9.5$) was nearly three times greater. As a consequence of its high mobility, the landslide crossed the entire 1-km-wide floodplain of the North Fork Stillaguamish River (Fig. 1 and Supplementary Figs. 1 and 2). As it overran the floodplain it demolished a neighborhood, buried highway SR 530, and caused 43 fatalities, ranking it second to only a 1985 event in Mameyes, Puerto Rico, as the worst land-slide disaster in U.S. history (cf. Jibson, 1992). Owing to its high mobility and the character of its variegated deposits, we describe the landslide at Oso as a debris avalanche-flow (DAF) (cf. Hungr et al., 2014). An alternative descriptive term, widely used in geotech-nical engineering, is flowslide (Mitchell and Markell, 1974; Dawson et al., 1998).

The Oso DAF (officially named the SR 530 Landslide by Wash-ington State) originated on a slope that was only 180 m high and inclined <20°, on average (Fig. 1c). The same slope had failed repeatedly in the past, most recently in 2006, when a landslide partially dammed the river and caused minor flooding. However, the 2006 landslide (known locally as either the Hazel or Steelhead landslide) and other historical landslides on the slope had not ex-hibited exceptional mobility (Fig. 1a). Elsewhere, landslides that transform into mobile, high-speed flows almost invariably begin

on slopes >20°, and initiation sites steeper than 30° are typical (Voight, 1978; Iverson et al., 1997). The great mobility of the Oso DAF therefore poses an important scientific problem. In this pa-per we aim to provide improved understanding of the Oso DAF and also to address broader issues concerning the mechanics of long-runout landslides and their implications for landslide hazard evaluation.

1.1. Meteorological and geological context

The Oso DAF occurred on a dry, sunny day, but it followed a long period of unusually heavy precipitation in the area. Well-established hydromechanical principles explain why most land-slides occur when weather has been wet, giving rise to high groundwater pressures (Lu and Godt, 2013). Analysis of data from a nearby weather station with an 86-year record indicates that the 45 days preceding the Oso DAF had been wetter than 98.2% of 45-day periods in the past (Table 1). Moreover, the 180 days pre-ceding the landslide had been wetter than 91% of similar periods in the past, and the four-year period that concluded on 31 March 2014 was the wettest such four-year period on record. Linear the-ory that relates rain infiltration rates to changes in groundwater pressure explains why the timescale for landslide onset can differ by weeks, months, or even years from the timescale of triggering rainfall (Iverson, 2000). However, as a result of the effects of hydro-logical nonlinearities and geological heterogeneities, quantitative

Table 1

Comparative long-term (1927–2014) precipitation summary. Data are from a rain gauge located at Darrington Ranger Station, about 16 km east of the Oso DAF site.

Precipitation ending in March 2014[a]				Greatest Precipitation in Record	
Duration of precipitation period (days)	Precipitation total (mm)	Ending date of precipitation period in March 2014	Prior precipitation totals exceeded	Greatest precipitation (mm)	Ending date of greatest precipitation
3	116	5 Mar 2014	98.9%	313	16 Jan 1974
7	224	9 Mar 2014	99.4%	418	22 Oct 2003
10	273	11 Mar 2014	99.4%	471	21 Oct 2003
14	317	16 Mar 2014	99.1%	554	13 Jan 2006
30	557	17 Mar 2014	99.2%	793	31 Jan 1953
45	683	22 Mar 2014	98.2%	968	30 Dec 1998
60	783	9 Mar 2014	96.1%	1153	30 Jan 1934
180	1634	21 Mar 2014	91.0%	2399	11 Apr 1974
365	2340	22 Mar 2014	77%	2745	21 Mar 1997
1-, 2-, 3-, 4-, and 5-year precipitation ending 31 March 2014					
365	2300	31 Mar 2014	72%	2725	31 Mar 1997
730	4563	31 Mar 2014	86%	5166	31 Mar 1998
1095	6948	31 Mar 2014	93%	7530	31 Mar 1999
1460	9495	31 Mar 2014	100%	9495	31 Mar 2014
1825	11,305	31 Mar 2014	94%	11,341	31 Mar 1999

[a] The first nine rows of tabulated data apply for ending dates with the greatest cumulative rainfall total prior to the 22 March occurrence of the Oso DAF. For example, the greatest 3-day rainfall in March 2014 ended on 5 March, not 22 March.

regional prediction of evolving groundwater pressures in landslide-prone slopes is in its earliest stages (Godt et al., 2008).

From a long-term geological perspective, renewed landslide activity on the slope where the Oso DAF originated was unsurprising (Miller and Sias, 1998). The slope had been periodically undermined by the North Fork Stillaguamish River (Fig. 1a). A geologic map of the area depicts abundant landslide deposits mantling a thick sequence of Pleistocene glacial till and outwash sediments that form the walls of the river valley (Dragovich et al., 2003). At the base of this stratigraphic sequence lies a glaciolacustrine silt-and-clay unit, similar to units in British Columbia, Canada, that have been prone to abrupt failure and landsliding (Fletcher et al., 2002; Hungr and Evans, 2004). Lidar imagery reveals that about 1 km west of the Oso DAF site, a large landslide deposit of unknown age spans and constricts the river floodplain (Haugerud, 2014). We informally refer to this deposit as the Rowan DAF (Supplementary Fig. 3), but no information exists regarding this prehistoric landslide's dynamics or the conditions that may have been responsible for its triggering. Thus, although geological evidence of past landslide activity in the vicinity of the Oso DAF was abundant, forecasting the DAF's timing – and more importantly, its mobility – would have required knowledge that was unavailable.

2. Methods

We use diverse methods to analyze the Oso DAF's mobility and dynamics. A preliminary analysis involves comparing values of morphometric mobility indices calculated for the Oso DAF with those for a large number of high-mobility landslides elsewhere. Use of lidar data and GIS plays an important role in this and other aspects of our study. Our most novel methodologies consist of inversion of broadband seismic data to analyze the sequence of events during landslide onset, and of numerical modeling to analyze alternative scenarios that could have unfolded once landsliding began. We supplement these methods with geological and eyewitness observations.

2.1. Lidar and GIS methods

Our mapping, morphometric measurements, and modeling of the Oso DAF benefited greatly from the availability of pre-event (2013) and post-event (2014) lidar topography as well as ortho-rectified aerial photography supplied by Snohomish County and

the State of Washington. Additional lidar data acquired in 2003 aided our understanding of the 2006 Hazel landslide. The most useful product from each set of lidar data is a digital elevation model (DEM), which provides elevations at regularly gridded points with 0.91 m horizontal resolution. Determining landslide surface areas and elevation changes between 2013 and 2014 entailed use of these DEMs and standard GIS methods.

A more elaborate GIS procedure involving landslide basal slip-surface reconstruction was needed to estimate the total Oso DAF volume, because the lower part of the landslide source area remained covered by landslide debris after motion concluded (Fig. 1b and c). We created three alternative basal slip surfaces by first drawing hypothetical 2-D longitudinal slip-surface profiles along five equally spaced transects spanning the landslide source area (Fig. 2). These profiles were constrained by matching the shapes of slip-surface exposures near the landslide headscarp, by requiring the toes of buried slip surfaces to terminate flush with the northwest bank of the North Fork Stillaguamish River, and by assuming that the curves joining the heads and toes of all profiles had shapes similar to those of logarithmic spirals (a standard theoretical shape for landslide profiles; Chen, 1975). We then created 3-D slip surfaces that passed through the 2-D profiles and also through the lateral landslide margins. This procedure yielded landslide volume estimates ranging from 7.3×10^6 m^3 to 9.2×10^6 m^3, and on that basis we chose 8.3×10^6 m^3 as a reasonable volume estimate (Fig. 2, Case B). Differencing the basal slip surface topography shown in Fig. 2, Case B with the surface topography derived from post-event lidar leads to the inference that more than half of the total Oso DAF volume (about 4.5×10^6 m^3) remained stranded in the source area after landslide motion concluded. We employed a similar basal surface reconstruction technique to estimate the volume of the prehistoric Rowan DAF.

2.2. Seismological methods

Use of seismic data to assess the behavior of landslides requires methodology that differs from that used to study tectonic earthquakes (Kanamori and Given, 1982; Allstadt, 2013; Ekström and Stark, 2013). Ground-shaking velocities containing many superposed frequencies can obscure the essential features of landslide dynamics. When observed using only far-field, long-period data, however, a landslide radiates seismicity equivalent to that of a single force pointing in the opposite direction of the accel-
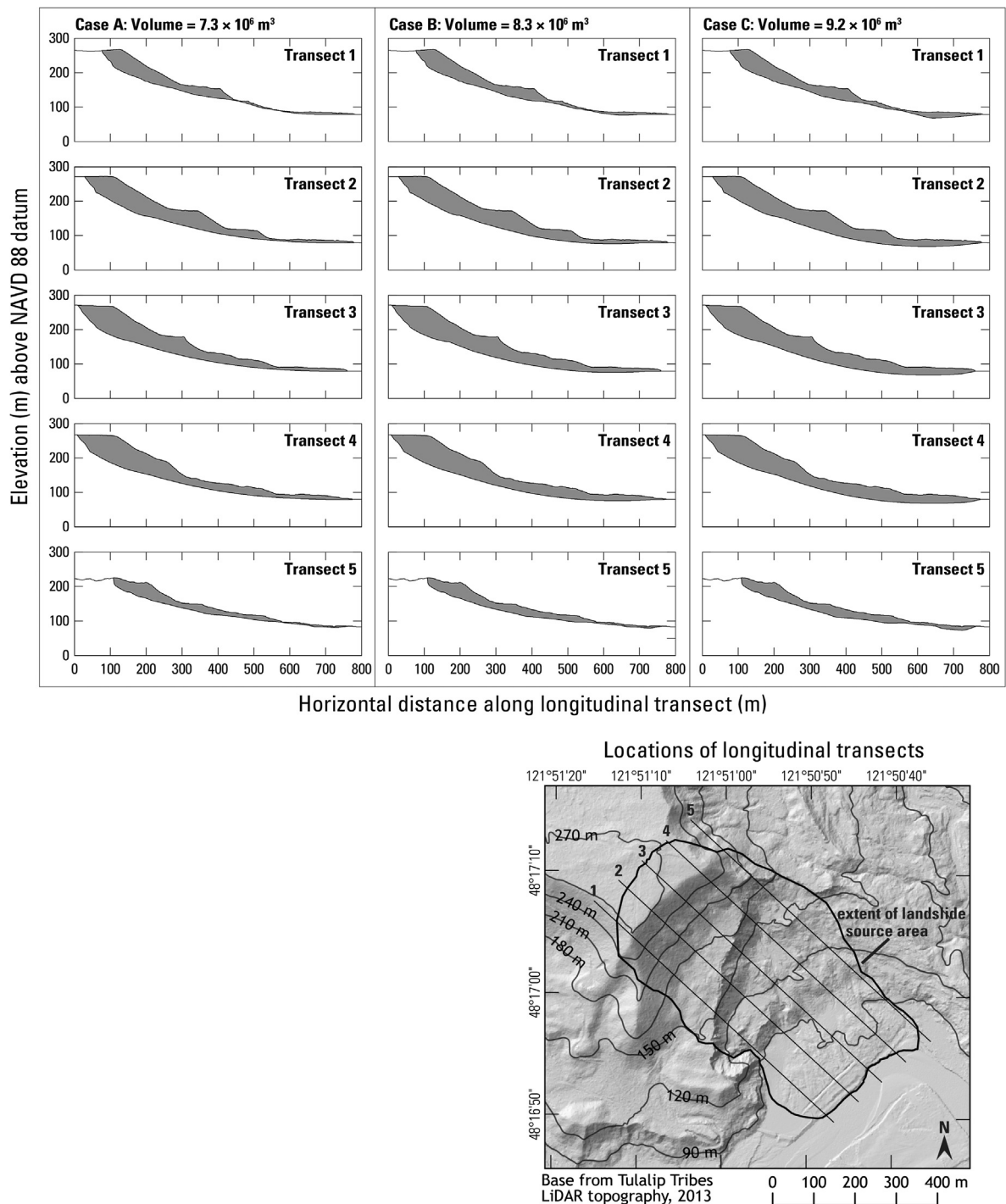
Fig. 2. Alternative sets of longitudinal slip-surface profiles constructed for the Oso DAF source area. Cases A, B, and C indicate source-area volumes of 7.3, 8.3 and 9.2×10^6 m^3, respectively. Case B was used to establish initial geometry for computational simulations.

eration of the landslide center of mass, with a magnitude equal to the acceleration times the mass (Kanamori and Given, 1982). Using methods detailed by Allstadt (2013), we inverted the long-period ($T = 30$–60 s) seismic data from 18 broadband seismic stations located 19 to 341 km from the Oso DAF site to obtain a time series of forces exerted on the earth by the moving landslide (Fig. 3A). The inversion model fits the data well, explaining 74% of the data variance (Fig. 3B), and this inversion is crucial for our interpretation of landslide chronology.

The Oso DAF and its seismic signals are smaller than those of any landslide previously analyzed using long-period seismic data

(Allstadt, 2013; Ekström and Stark, 2013). Thus, the amplitude of the force history is at times comparable to the noise level. However, Allstadt (2013) found that the main features of the landslide force history can be retrieved even with a noise level as high as 40% of the peak signal amplitude. In order to adapt the inversion methods of Allstadt (2013) to a landslide with a relatively low signal-to-noise ratio, we added equations to the model to set all forces equal to zero prior to $t = 0$ (the time of landslide onset). The absolute time of $t = 0$ was found iteratively and the equations were tapered to avoid spikes in the signal that appeared if the constraint was suddenly released without tapering. Addition-
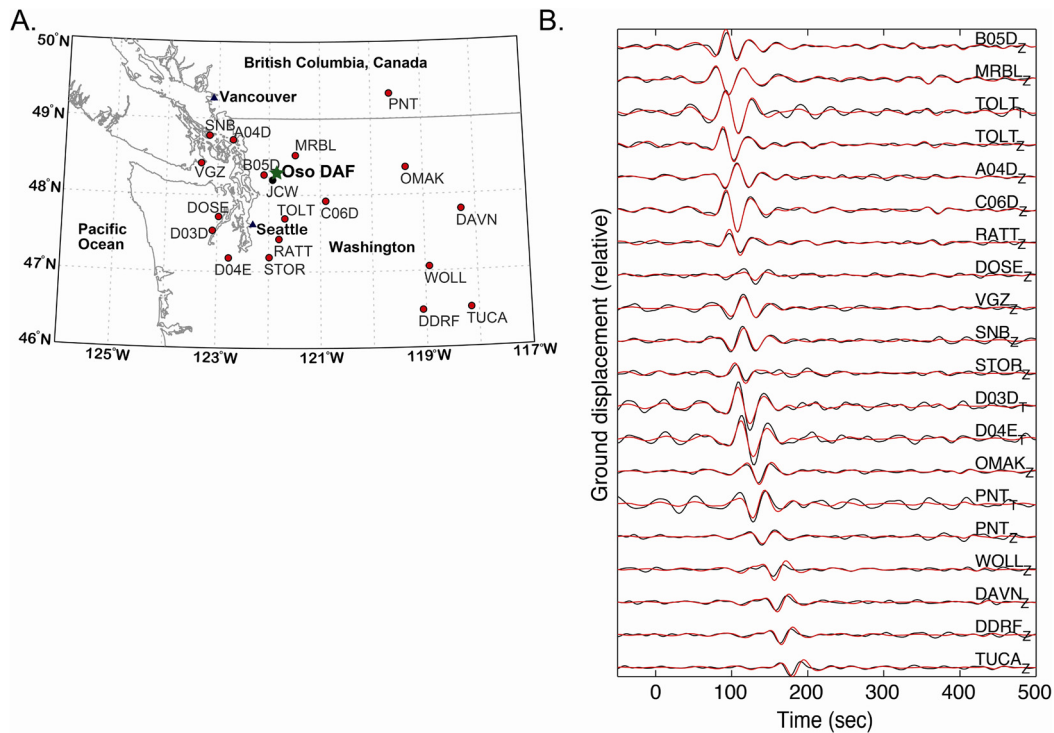
Fig. 3. Seismometer stations that provided data used to extract Oso DAF seismic source characteristics. A: Geographic locations of the Oso DAF site, the closest short-period seismometer (JCW), and the 18 broadband seismometers that supplied data used in our inversion model of landslide force history. B: Comparison of best-fitting inversion model (red) with data (black) from broadband seismometers identified by station name. Subscripts Z and T on station names refer to vertical component and transverse component of ground displacement, respectively. (For interpretation of the references to color in this figure legend, the reader is referred to the web version of this article.)

ally, we did not require that the net forces exerted on the Earth by the landslide sum to zero over the duration of the event. Although a zero force sum is theoretically correct, the relatively high noise level makes meeting this condition unrealistic and could introduce artifacts. We weighted the seismic data from all stations equally when performing our inversion, but the long-period data from most of the horizontal motion components were too noisy to use in this procedure. Therefore, for most stations we used only the vertical components. Tests of the inversion method on the $\sim 5 \times 10^7$ m^3 Mount Meager, British Columbia, landslide of 2010 showed that use of only vertical components did not significantly alter the results (Allstadt, 2013), and it appears unlikely to do so in this case as well. Further discussion of our seismological methods and the influence of the signal-to-noise ratio is provided in Appendix A.

2.3. Numerical modeling methods

To investigate effects of initial sediment conditions on the mobility of the Oso DAF, we performed alternative numerical simulations of the event by using our newly created software package, D-Claw. The physical, mathematical, and computational basis of D-Claw, as well as tests of model predictions against well-constrained experimental data, are described in detail elsewhere (Iverson and George, 2014; George and Iverson, 2014). Our simulations of the Oso event represent the first application of D-Claw to natural phenomena.

A novel feature of D-Claw is its ability to seamlessly simulate landsliding during both the onset of slope failure and subsequent landslide runout. The model employs a shock-capturing finite-volume method and adaptive mesh refinement (AMR) to solve a hyperbolic system of five depth-integrated partial differential equations derived by combining continuum conservation laws with concepts from soil mechanics, fluid mechanics, and grain–fluid mixture mechanics (Iverson and George, 2014; George and

Iverson, 2014). In addition to computing evolving values of two components of landslide velocity and the landslide thickness, D-Claw computes the coevolution of the solid volume fraction m and basal pore-fluid pressure. Evolving basal pore pressure influences landslide mobility though application of the Coulomb friction rule and effective-stress principle, which are widely used in landslide and debris-flow mechanics (Iverson, 1997; Iverson et al., 1997; R.M. Iverson et al., 2010).

Boundary conditions used by D-Claw consist of a DEM representing pre-event topography as well as a DEM representing the inferred geometry of the basal landslide slip surface (Fig. 2, Case B). Initial conditions consist of the initial landslide volume and geometry inferred from differencing these DEMs, as well as initial values of two material properties (bulk compressibility and hydraulic permeability) that evolve in response to evolution of the solid volume fraction. Section 3.4 reports these values as well of those of all other model parameters used in our computations.

3. Results

3.1. Landslide mobility indices

The mobility of the Oso DAF can be placed in a worldwide context by using well-established landslide mobility indices (Fig. 4). Many studies have shown that values of the best-known mobility index, L/H, increase as the volume V of high-speed landslides increases (e.g., Scheidegger, 1973; Corominas, 1996; Legros, 2002). On a graph of L/H as a function of V, the Oso DAF plots above a line depicting the previously known upper mobility limit for debris and rock avalanches, including extremely mobile avalanches with volcanic origins (i.e., orange line in Fig. 4a). Aside from the Oso DAF, the only landslides with L/H values that plot above this mobility limit fall into one of two categories. One category includes flowslides composed of sensitive marine clays or uncompacted mine tailings, which are materials with loose, metastable
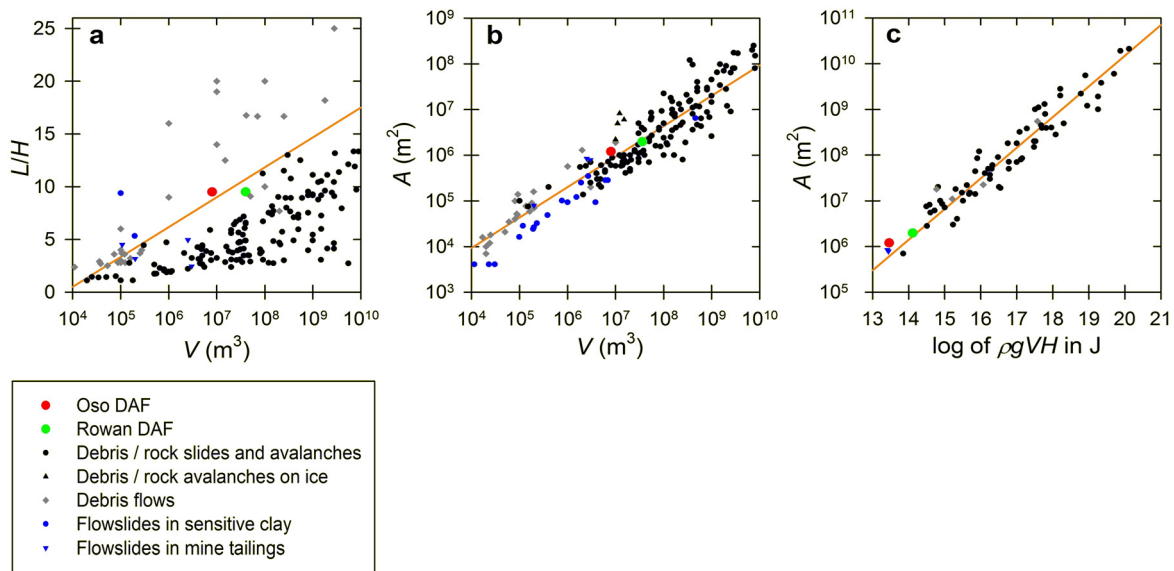
Fig. 4. Mobility-index graphs for diverse high-speed landslides, including worldwide data from several sources as well as data for the Oso DAF and the informally named Rowan DAF, a prehistoric landslide about 1 km west of the Oso DAF site (Supplementary Fig. 3). Each graph displays data for somewhat different sets of landslides, because few studies report all morphometric quantities needed to compile all three graphs. Orange line in panel a depicts previously known upper-bound behavior for rock and debris avalanches. Orange line in panel b is the fitted equation $A = 20V^{2/3}$ determined from physical and statistical constraints by Griswold and Iverson (2008). Orange line in panel c is the empirical power-law fit of Dade and Huppert (1998). Data sources for panel a are Carasco-Nunez et al. (1993), Corominas (1996), Iverson (1997), Dawson et al. (1998), Legros (2002), and Zanchetta et al. (2004); for panel b are Mitchell and Markell (1974), Dawson et al. (1998), and Griswold and Iverson (2008); for panel c are Iverson (1997), Dade and Huppert (1998), Dawson et al. (1998), Iverson et al. (1998) and Griswold and Iverson (2008).

structures that are highly susceptible to liquefaction during slope failure. The other category comprises debris flows, the largest and most-mobile of which originate on volcanoes. Unlike virtually all large debris flows, however, the Oso DAF traveled across a nearly flat surface. There was no channelizing topography to focus its momentum and thereby enhance its L/H value.

Another mobility index is the ratio $A/V^{2/3}$, where A is the planimetric area covered by a landslide path (Iverson et al., 1998; Legros, 2002; Griswold and Iverson, 2008). This index ignores the influence of H but accounts for effects of topography that channelizes runout. On a log–log graph of A as a function of V, data for rock and debris avalanches as well as non-volcanic debris flows loosely follow a power-law trend described by $A = 20V^{2/3}$, where the "mobility coefficient" 20 is calibrated statistically (Griswold and Iverson, 2008) (Fig. 4b). The Oso DAF had $A \approx 1.2 \times 10^6$ m^2 and a mobility coefficient $A/V^{2/3} \approx 30$, implying that it impacted an area about 50% larger than expected for an average rock or debris avalanche or debris flow of similar volume. Fig. 4b shows that mobility coefficients defined by $A/V^{2/3}$ values can vary widely, however. Differences in H among landslides are one obvious source of this variation.

A third index of landslide mobility accounts for the influence of H on A by using a proxy for landslide potential energy (Fig. 4c). This proxy is defined as $\rho g V H$, where g is the magnitude of gravitational acceleration and ρ is the landslide bulk density (Dade and Huppert, 1998). For the Oso DAF we use $\rho = 2000$ kg/m^3 (based on our measurements of eight core samples), and this value yields $\rho g V H \approx 2.8 \times 10^{13}$ J. Adding this data point to a log–log graph of A as a function $\rho g V H$ shows that the area inundated by the Oso DAF plots about 1/3 log cycle above the mean power-law trend established for large, high-mobility landslides elsewhere (Dade and Huppert, 1998) (Fig. 4c). A clear reason for this offset is that, in comparison to typical high-mobility landslides, the Oso DAF began at a site with modest topographic relief and relatively little potential energy.

3.2. Landslide chronology

The sequence of events during the onset of the Oso DAF may have influenced landslide mobility. Detectable landslide motion began at 10:36:33 AM local time (17:36:33 UTC) according to our inversion of broadband seismic data (Fig. 5). No seismic evidence exists of an external earthquake trigger or other identifiable precursor.

Landslide motion initially produced only a long-period seismic signal and no measured high-frequency energy radiation (Fig. 5A interval 1, beginning at $t = 0$ s). This seismic signature is indicative of acceleration of a relatively coherent mass of material. Data inversion that estimates the magnitude, azimuth, and duration of the forces associated with this signal implies that this initial landslide did not spontaneously transform into the DAF (Fig. 5B and Supplementary Table 1). Instead, the landslide began to decelerate, but its deceleration was interrupted at $t \approx 50$ s by a pair of larger, long-period force pulses that were accompanied by radiation of considerable high-frequency seismic energy (Fig. 5A, C, interval 2). Taken together, these data imply that after nearly a minute of relatively moderate motion, the landslide accelerated significantly, and the moving material became highly agitated. The duration of the associated high-frequency ground shaking was about 100 s. Another prominent seismic event, beginning at $t = 310$ s in Fig. 5C, also radiated considerable high-frequency energy (Fig. 5A, interval 5–6). However, it generated a weak and steeply dipping long-period force, implying that the seismic source was a relatively small mass of disaggregated material falling almost vertically. This phase of activity probably produced the "secondary debris fall" deposit identified in Fig. 1b and Supplementary Fig. 2.

Eyewitness accounts of the Oso DAF corroborate seismic records of the landslide chronology. We obtained a key eyewitness account a few days after the event from a man who had been standing on a fluvial terrace just west of the DAF path, with a clear view overlooking the adjacent North Fork Stillaguamish River. The man was first alerted to the event by a roaring noise, which he described as similar to that of "low-flying aircraft." He could not see its cause,
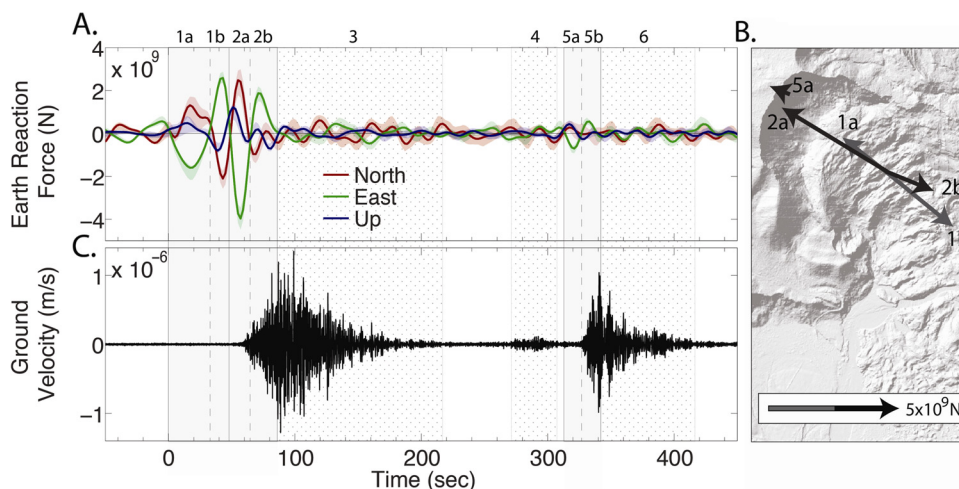
Fig. 5. Seismic timeline of the Oso DAF event sequence. Zero time corresponds to the start of the first signal on 22 March 2014 at 17:36:33 UTC. A: Force history of the Earth's reaction to the landslide, obtained from inversion of long-period ($T = 30$–60 s) seismic data from 18 broadband stations (Fig. 3); 95% confidence limits are indicated by light colored fill. B: Post-event lidar image of Oso DAF source area with superposed vectors indicating directions and magnitudes of peak Earth reaction forces during each time interval identified in A. C: The contemporaneous high-frequency (1–20 Hz) seismic energy recorded at the closest short-period seismic station, JCW, located 11.5 km from the landslide, adjusted for differing seismic wave travel times to align with the force history (see Fig. 3 and Appendix A).

however, because terrain and trees blocked his view of the landslide source area. At this time he saw no landslide activity in the vicinity of the river. The initial roaring noise gradually diminished, and tens of seconds passed before another loud noise developed and the man saw the river "tossed in the air," and "turning black" in color. He then saw "a wall of turbulent earth" moving southeastward, with a height he estimated as "100 feet overhead" and a speed he estimated as "100 miles per hour."

Our interpretation of the landslide seismicity and of the eyewitness account is that motion of a relatively coherent landslide on a lower segment of the slope occurred first, and gradually withdrew support from a mass above it. This stage of activity lasted tens of seconds, and likely involved remobilization of remnants of 2006 Hazel landslide material (Fig. 1a). It may have produced a roaring noise by setting trees astir, like a strong wind does in a forest. This initial stage of landslide motion was limited, however, and did not extend to the river. As the initial landslide decelerated, retrogressive collapse of the upslope bluff occurred (seismic interval 2a in Fig. 5A, C), instigating a chain of events leading to the high-speed DAF. Although the upper part of the collapsed bluff ultimately remained stranded below the headscarp as a slump block (Fig. 1b and Supplementary Figs. 1 and 2), the lower part of the collapsed bluff traveled farther and may have exerted a large compressional force on wet material downslope, producing a potential for undrained loading and accentuating the possibility of sediment liquefaction (cf. Hutchinson and Bhandari, 1971; Iverson et al., 2011). The details of liquefaction and its effect on landslide dynamics during the crucial next few seconds cannot be inferred from seismological or eyewitness observations. However, high-speed motion of the disaggregating DAF ensued, and appears to have lasted about 100 s based on the duration of high-frequency seismic energy radiation recorded at the nearest station (Fig. 5C).

3.3. Landslide liquefaction evidence

Abundant field evidence indicates that widespread basal liquefaction occurred and likely enhanced the mobility of the Oso DAF. Most of the DAF deposit south of the river consisted of hummocks (mounds) of unliquefied source material, and the tops of some hummocks were covered by fallen trees and intact remnants of forest floor vegetation (Fig. 6). Similar hummocks are characteristic of debris-avalanche deposits formed when relatively strong material rides atop a weaker (e.g., liquefied) basal layer (Paguican

Fig. 6. Photographs of some key features of OSO DAF deposit. Main photo shows a brown pool of persistently liquefied muddy sand containing a sand boil, which lies between ochre-toned hummocks. Yellow notebook on ground near sand boil is 19 cm long. Fern at lower right was rafted into place atop an intact block of debris avalanche material. Landslide headscarp is visible in distance, about 1.2 km away. Inset photo shows oblique aerial perspective of the Oso DAF deposit viewed from the east, with red dot that identifies location of sand boil photo. USGS photos by M.E. Reid on 1 April (inset photo) and 14 April (sand boil photo) 2014. (For interpretation of the references to color in this figure legend, the reader is referred to the web version of this article.)

et al., 2014). Scattered amid the debris-avalanche hummocks were many sand boils as well as pools of muddy sand that remained liquefied for weeks following landslide motion. Sand boils, in particular, provide evidence of liquefied material at depth in the DAF (Fig. 6).

The leading edge of the DAF produced the most water-rich, pervasively liquefied part of the deposit. The composition of this distal deposit indicated that it was emplaced by a debris flow, which was heavily freighted with wood and other objects entrained in transit (Supplementary Fig. 4). Eyewitness accounts, distal splash deposits, and stratigraphic relationships indicated that parts of this debris flow ran up and reflected off the southern valley wall and then underwent tens to hundreds of meters of retrograde (i.e., predominantly northward) motion. During this flow reversal the

Table 2
Values of all parameters used in D-Claw numerical simulations.

Material property	Oso DAF simulation with $m_0 - m_{crit} = -0.02$	Alternative simulation with $m_0 = m_{crit}$
Sediment basal friction angle, ϕ_{bed} (degrees)	36	36
Initial sediment porosity, $1 - m_0$	0.38	0.36
Static critical-state sediment porosity, $1 - m_{crit}$	0.36	0.36
Initial sediment hydraulic permeability, k_0 (m^2)	1.0×10^{-8}	1.0×10^{-8}
Pore fluid (muddy water) mass density, ρ_f (kg/m^3)	1100	1100
Sediment grain mass density, ρ_s (kg/m^3)	2700	2700
Proportionality coefficient,[a] a	0.03	0.03
Pore-fluid (muddy water) viscosity, μ (Pa s)	0.005	0.005

[a] Coefficient a is used in D-Claw for scaling the bulk elastic compressibility of the sediment-fluid mixture, α (Pa^{-1}). This compressibility is given by the formula $\alpha = \frac{a}{m(\sigma_e + \sigma_0)}$, where σ_e is the ambient basal effective stress and σ_0 is a baseline effective stress. In all simulations we set $\sigma_0 = 1000$ Pa. See Iverson and George (2014) and George and Iverson (2014) for details.

debris flow overrode the already-emplaced, hummocky deposit of the debris avalanche, creating an extensive but thin "debris-flow veneer" deposit (Fig. 1b and Supplementary Fig. 2). In most places we observed this deposit in the weeks following its emplacement, it was less than 0.3 m thick, although pockets of liquefied debris-flow sediment >1 m thick existed. Most of the debris-flow deposit was subsequently removed during excavation and highway reconstruction work, but we estimate that the volume of the debris-flow portion of the Oso DAF was roughly 200,000 m^3 on the basis of its ~0.4 km^2 surface area and an assumed average thickness of 0.5 m. Thus, although water-rich, woody debris-flow material was the first to traverse the floodplain, its volume probably was less than 3% of the DAF total.

The leading-edge debris flow may have resulted from displacement and entrainment of water by the DAF when it encountered the North Fork Stillaguamish River. The eyewitness report summarized in Section 3.2 supports this inference. On the basis of the river's average cross-sectional area and stream-gauge records for 22 March 2014, we estimate that the section of river encountered by the landslide contained about 50,000 m^3 of water. Debris flows typically have water contents ranging from 20% to 60% by volume (Iverson, 1997). Therefore, incorporation of 50,000 m^3 of water by the leading edge of a fast-moving, wet landslide could have been sufficient to generate a 200,000 m^3 debris flow. Scour and liquefaction of wet floodplain sediment by the surging mass could also have been a contributing factor (cf. Iverson et al., 2011).

3.4. Numerical simulations of landslide dynamics and mobility

A crucial question regarding the Oso DAF concerns whether prevailing conditions at the site made landslide liquefaction and high mobility nearly inevitable – or whether the landslide process could have unfolded differently. Direct field evidence that could help answer this question is largely gone (having been destroyed by the landslide), and seismological evidence lacks adequate resolution. However, the question can be addressed in a mechanistic way by performing alternative numerical simulations of the landslide's dynamics. Our simulations are not intended to recreate the precise details of the slope-failure process at Oso, but rather to demonstrate how differing styles of landslide behavior could have developed as irreversible slope failure began and landslide motion proceeded.

To simulate the dynamics of the DAF, as well as those of an alternative landslide scenario, we use D-Claw with parameter values estimated from measurements on sand-rich sediment mixtures similar to those in much of the Oso DAF source area (Iverson et al., 2000; R.M. Iverson et al., 2010). However, the precise values of parameters are less important than the fact that only one of the parameters, the initial porosity of water-saturated sediment (expressed as $1 - m_0$, where m_0 is the initial solid volume fraction), has a value that varies between our alternative simulations (Table 2). In each simulation landslide motion is instigated by grad-

ually increasing the basal pore-water pressure everywhere within the slope until failure nucleates at the weakest point, and failure then spreads to adjacent areas.

Modeled landslide dynamics exhibit a very sensitive dependence on the value of m_0. If saturated sediment has $m_0 < m_{crit}$ (where m_{crit} is a critical-state solid volume fraction that sediments tend to attain when subjected to large, quasi-static shear strains; Schofield and Wroth, 1968), then sediment contraction occurs during the onset of slope failure, and basal pore-water pressures begin to rise in response. Contraction and pore-pressure growth may also be enhanced by compression caused by motion of material encroaching from upslope. Feedbacks involving coupled evolution of mass and momentum distributions as well as those of porosity and basal pore pressure then determine whether liquefaction occurs and influences landslide dynamics. The phenomenology and theory of this type of feedback mechanism are well-known (Iverson, 2005; Pailha and Pouliquen, 2009), but D-Claw is the first computational landslide dynamics model to incorporate it fully (Iverson and George, 2014; George and Iverson, 2014).

Our model results illustrate bifurcating scenarios that could have unfolded when the slope began to fail at Oso. A simulation that employs $m_0 = m_{crit}$ produces behavior in which a relatively slow landslide occurs, crosses the river, and then moves little farther (Fig. 7a, b, c and Supplementary Movie 1). This behavior is similar to that of the 2006 Hazel landslide at Oso (Fig. 1a). By contrast, a simulation that employs $m_0 - m_{crit} = -0.02$ produces behavior in which widespread basal liquefaction develops and leads to runaway acceleration and high landslide mobility (Fig. 7 a, d, e and Supplementary Movie 2).

Model results obtained with $m_0 - m_{crit} = -0.02$ show that a fast-moving surge of landslide debris crosses the entire 1-km-wide North Fork Stillaguamish River floodplain in about one minute, and that debris then continues spreading laterally (Fig. 7a, d, e and Supplementary Movie 2). This timing is consistent with the duration of high-frequency ground shaking observed at Oso (Fig. 5C). As observed in the field, some of the modeled distal debris encounters the southern valley wall and then reverses direction and flows northward. Other distal debris continues to creep laterally outward long after most motion ceases (Supplementary Movie 2). Within 10 min of landslide onset, the total kinetic energy of the moving debris diminishes to <0.004% of its peak value ($\sim 5 \times 10^{12}$ J). The final extent of the modeled deposit resembles that of the deposit of the Oso DAF (Fig. 8).

4. Discussion

Scientific understanding of the behavior of large, high-mobility landslides is hampered by their capricious timing and by the risks they pose to investigators and instrumentation. Nevertheless, perhaps more than any previous high-mobility landslide, the Oso DAF affords strong clues about mobility because of abundant empirical
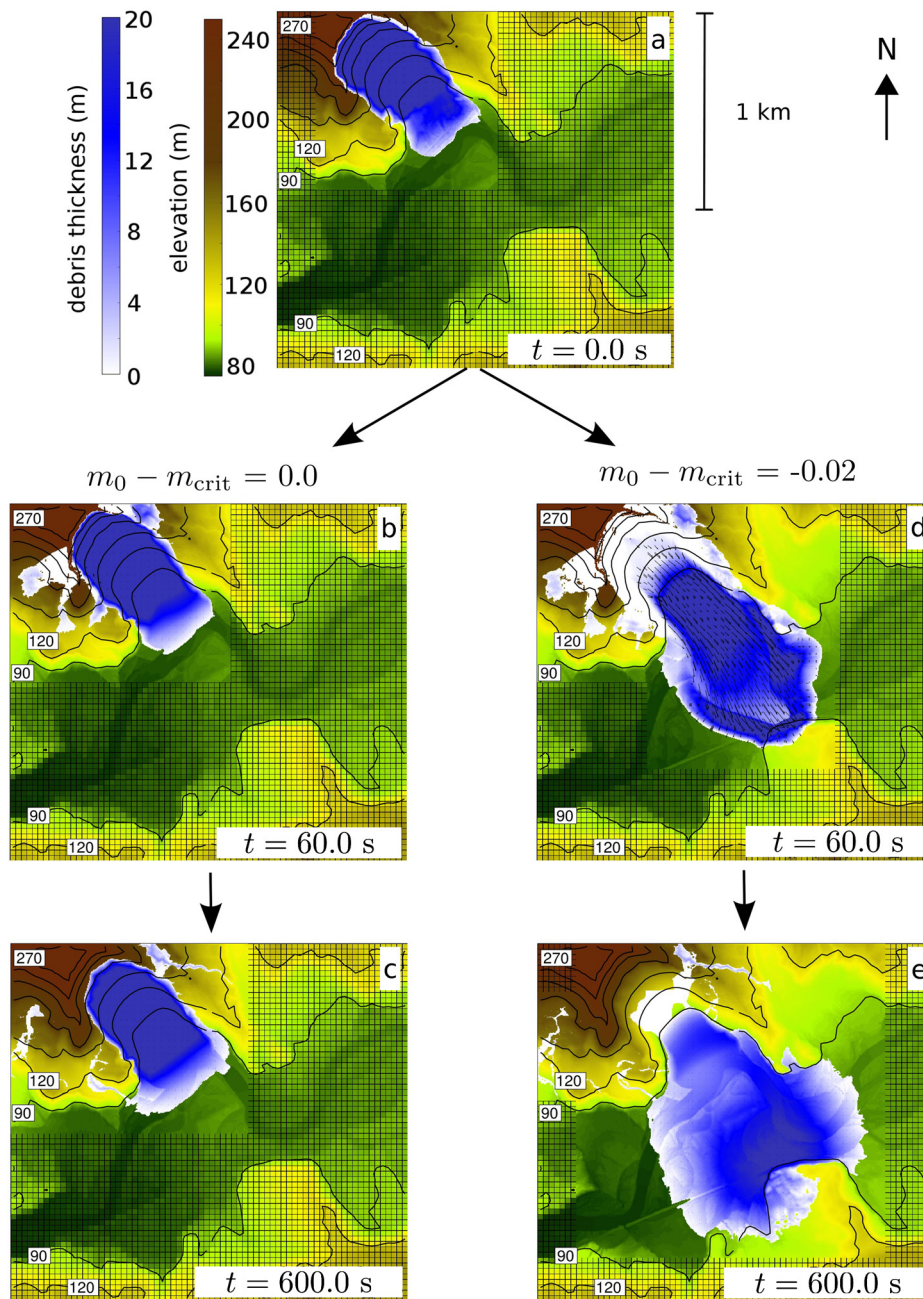
Fig. 7. Numerical simulation results illustrating bifurcating landslide mobility scenarios at Oso. a: Initial configuration of 8.3×10^6 m^3 of static landslide material used in each simulation (see Fig. 2). b and c: Simulated landslide motion with $m_0 = m_{crit}$ (not leading to liquefaction). d and e: Simulated landslide dynamics with $m_0 - m_{crit} = -0.02$ (leading to widespread basal liquefaction). Supplementary movies 1 and 2 provide animated versions of these simulations. Labeled contours show elevations in m above NAVD 88 datum. Evolving orthogonal grid lines result from adaptive mesh refinement (AMR) during computations.

evidence combined with modern methods of seismic data processing and numerical simulation.

Our simulations of the DAF and of an alternative landslide scenario indicate that basal liquefaction and high landslide mobility develop only if wet sediment has $m_0 < m_{crit}$, where m_0 is the initial solid volume fraction and m_{crit} is the static, critical-state solid volume fraction. In this case, sediment undergoes pore-space contraction during the early stages of landslide motion. Geological processes that could have produced conditions with $m_0 < m_{crit}$ in the Oso DAF source area include sediment dilation during prior episodes of landsliding at the site (including the first stage of landsliding on 22 March 2014), long-term volumetric relaxation of glacially unloaded fine-grained sediments at the base of the land-

slide, or slow, shear-induced disaggregation of those sediments (cf. Hungr and Evans, 2004; Jibson, 2006; N.R. Iverson et al., 2010). Further field investigations and laboratory testing may help determine which of these possibilities are most plausible.

Sediment liquefaction at the base of large landslides differs fundamentally from liquefaction due to earthquake shaking. It is a difficult process to replicate experimentally, because several aspects of landslide behavior can be scale-dependent. Nevertheless, experiments conducted at the largest scales reveal three key phenomena. First, landsliding of wet, loosely packed sediment that contracts as it fails can be accompanied by abrupt increases in basal pore-water pressure (Iverson et al., 1997, 2000; Moriwaki et al., 2004; Ochiai et al., 2007). Second, wet sediment that is rapidly compressed by
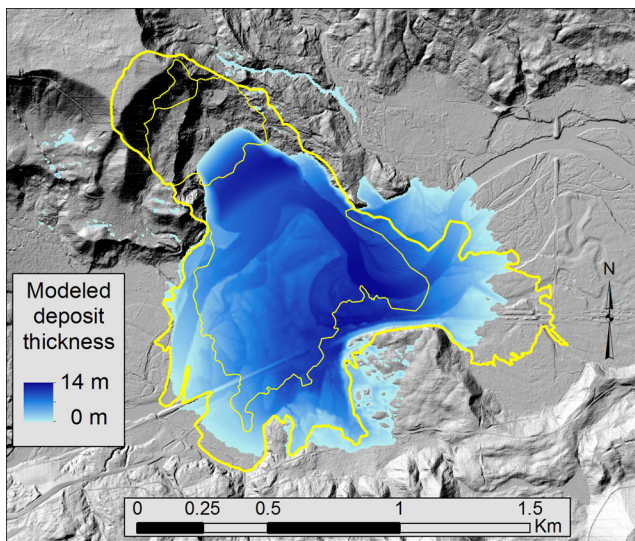
Fig. 8. Comparison of modeled and observed deposit extent superposed on shaded relief map derived from 2013 lidar topography. Margin of area affected by the Oso DAF (heavy yellow line) is superposed on D-Claw model output that shows computed distribution of Oso DAF deposit (blue shaded area) after 30 min of simulated landslide motion. Lighter yellow lines depict boundaries of depositional units identified in Fig. 1b and Supplementary Fig. 2. (For interpretation of the references to color in this figure legend, the reader is referred to the web version of this article.)

material moving from upslope can develop high pore pressures, even if the sediment is highly permeable (Iverson et al., 2011; Reid et al., 2011). Finally, high pore pressures may dissipate slowly in rapidly moving, water-laden landslides that contain even small amounts of silt and clay, and the moving sediment–water mixtures consequently can remain highly mobile (Iverson, 1997; R.M. Iverson, 2010). All of these processes are represented in our numerical simulations, and all may have played a role in causing high landslide mobility at Oso.

Investigations of historical, high-mobility landslides elsewhere have indicated that some can exhibit hybrid behavior in which drier, stronger material rides atop a wetter, liquefied basal layer. Events of this type include the Ontake, Japan, debris avalanche of 1984 (Voight and Sousa, 1994), the Nomash River, Canada, landslide of 1999 (Hungr and Evans, 2004), and also the largest subaerial landslide in recorded history: the 2.5×10^9 m^3 rockslide/debris avalanche that unleashed a lateral volcanic blast during the 1980 eruption of Mount St. Helens (MSH), Washington, USA (Voight et al., 1983). Discharging from several sources in the freshly emplaced, hummocky MSH debris avalanche deposit was a 1.4×10^8 m^3 lahar, a liquefied volcanic debris flow (Major et al., 2005). The hummocky Oso DAF deposit has many traits similar to those of the 1980 MSH debris-avalanche deposit, although the debris flow at the Oso DAF distal margin appears to have had a distinctive origin.

In some places the leading-edge debris flow at Oso traveled tens of meters farther than did the debris-avalanche material behind it. However, we infer that the relatively small debris flow ($\sim$200,000 m^3) was probably pushed forward by the avalanche. To our knowledge, no similarly small debris flow moving across a nearly flat surface has produced runout distances and inundation areas as large as those produced by the leading edge of the Oso DAF.

5. Conclusions

Our findings lead us to conclude that the Oso disaster was severe not because a large landslide occurred, but because the Oso DAF was unusually mobile. Landslides might exhibit high mobili-

ties for diverse reasons, but an abundance of empirical and computational evidence indicates that liquefaction of wet basal sediment played a pivotal role at Oso. Such liquefaction is by no means inevitable when a wet landslide occurs, however. Liquefaction requires a combination of initial conditions and dynamics than enables pore-water pressures to be driven to near-lithostatic levels as potential energy transforms to kinetic energy during landslide motion (Iverson, 1997). Seismological evidence indicates that rapid compressional loading of already-unstable wet sediment by material collapsing from upslope may have been an important factor contributing to liquefaction at Oso. More broadly, however, our numerical simulations indicate that dynamical feedbacks involving coevolution of landslide momentum, thickness, porosity, and basal pore pressure can cause a bifurcation in landslide behavior in response to small differences in initial conditions. Simulation results indicate that basal liquefaction and high mobility may not have developed at Oso if the initial porosity of water-saturated sediment had been only slightly smaller. A strong dependence of landslide mobility on nuanced differences in initial conditions – which themselves depend on geological and meteorological contingencies – has wide implications. It poses a significant challenge for quantitative landslide hazard evaluation, which differs fundamentally from landslide hazard recognition.

Appendix A. Seismological details

In order to better understand the influence of seismic noise on our inversion solution and thus the degree to which we can interpret the Oso force history, we followed the methods of Moretti et al. (submitted for publication) to compute 95% confidence intervals using a jackknife technique. We discarded half of the data randomly and recomputed the inversion, repeated this 200 times and used bounds around the middle 95% of the solution points at each time interval as 95% confidence intervals. The result of this analysis, indicated by light colored shading around the time series of each component on Fig. 5A, shows that the solution is very stable except for the amplitude of the initial acceleration pulse (interval 1a in Fig. 5), which is the lowest amplitude part of the main signal. The small force associated with interval 5 in Fig. 5 is at the same level as the noise, but the confidence intervals narrow at that point and are significantly different from zero, implying that the signal is real. Supplementary Table 1 summarizes the magnitudes, angles, and azimuths of the peak of each force pulse, as well as the range of uncertainties. The empirical estimates of landslide mass listed in Supplementary Table 1 were computed using relations from Ekström and Stark (2013). The possible ranges of mass were computed by imposing a maximum possible range of accelerations of 0.05 to 2.9 m/s^2. The upper limit is based on the maximum acceleration possible on a 17° slope (the estimated mean slope of the basal landslide failure surface shown for Case B in Fig. 2) without any friction.

In order to align the force history with the timing of the arrival of the high-frequency seismic energy as recorded at the closest seismic station (JCW, Fig. 3B), we needed to estimate the travel time for high-frequency ($\sim$1–5 Hz) waves from the source area to reach JCW. This travel time was measured from a seismic recording

of a headscarp debris fall on 25 April 2014, which was directly witnessed by a geologist on site and was big enough to be recorded at station JCW as well as by seismometers deployed directly adjacent to the landslide to monitor post-event activity. These recordings revealed a maximum travel time of 6.4 seconds (equivalent to an apparent wave speed of ~1800 m/s). This is a maximum speed because the first arrivals of seismicity at JCW were emergent, so that the exact arrival time could not be ascertained.

An important feature of the high-frequency part of the signal is that the first stage of the Oso DAF signal, interval 1 in Fig. 5, does not have any accompanying high frequencies above the noise level at the closest seismic station (JCW). Therefore, the process that generates strong high frequencies, which is probably agitated flow – with many rapid, small-scale momentum exchanges – was minimal during this initial phase. The high frequencies don't emerge until the end of the 2a acceleration phase shown in Fig. 5, and they peak after the deceleration phase (2b). This peak late in the event is not unprecedented; higher frequencies tend to be produced most readily by agitated flow as well as by an increased landslide frictional work rate (Schneider et al., 2010; Allstadt, 2013), both of which would be more pronounced after the DAF left the source area. We searched through archived seismic data for seismic signals from the 2006 Hazel landslide (Fig. 1a), and concluded that, like the initial stage of 2014 DAF, it did not generate any observable high-frequency signal observable at the nearest station, JCW.

The long-period deceleration phase in interval 2b of Fig. 5 is above the noise level only on the east component, suggesting it is most likely due to the change in direction of the dominant DAF motion from SE to S. The absence of a strong deceleration phase on the other components is not surprising because at this stage the landslide material had largely liquefied, with forces spread out in space and time and directed in opposing directions at various locations.

Appendix B. Supplementary material

Supplementary material related to this article can be found online at http://dx.doi.org/10.1016/j.epsl.2014.12.020.

References

Allstadt, K., 2013. Extracting source characteristics and dynamics of the August 2010 Mount Meager landslide from broadband seismograms. J. Geophys. Res. 118, 1472–1490. http://dx.doi.org/10.1002/jgrf.20110.

Carasco-Nunez, G., Vallance, J.W., Rose, W.I., 1993. A voluminous avalanche-induced lahar from Citlaltépetl Volcano, Mexico: implications for hazard assessment. J. Volcanol. Geotherm. Res. 59, 35–46.

Chen, W.F., 1975. Limit Analysis and Soil Plasticity. Developments in Geotechnical Engineering, vol. 7. Elsevier, Amsterdam.

Corominas, J., 1996. The angle of reach as a mobility index for small and large landslides. Can. Geotech. J. 33, 260–271.

Dade, W.B., Huppert, H.E., 1998. Long-runout rockfalls. Geology 26, 803–806.

Dawson, R.F., Morgenstern, N.R., Stokes, A.W., 1998. Liquefaction flowslides in Rocky Mountain coal mine waste dumps. Can. Geotech. J. 35, 328–343.

Dragovich, J.D., Stanton, B.W., Lingley, W.S., Griesel, G.A., Polenz, M., 2003. Geologic map of the Mount Higgins 7.5 minute quadrangle, Skagit and Snohomish Counties, Washington. Washington State Div. Geol. Earth Res. Open-file report 2003-12.

Ekström, G., Stark, C.P., 2013. Simple scaling of catastrophic landslide dynamics. Science 339, 1416–1419. http://dx.doi.org/10.1126/science.1232887.

Farin, M., Mangeney, A., Roche, O., 2014. Fundamental changes of granular flow dynamics, deposition and erosion processes at high slope angles: insights from laboratory experiments. J. Geophys. Res., Earth Surf. 119, 504–532. http://dx.doi.org/10.1002/2013JF002750.

Fletcher, L., Hungr, O., Evans, S.G., 2002. Contrasting failure behavior of two large landslides in clay and silt. Can. Geotech. J. 39, 46–62.

George, D.L., Iverson, R.M., 2014. A depth-averaged debris-flow model that includes the effects of evolving dilatancy: 2. Numerical predictions and experimental tests. Proc. R. Soc. Lond. Ser. A 470, 20130820. http://dx.doi.org/10.1098/rspa.2013.0820.

Godt, J.W., Baum, R.L., Schulz, W.H., Savage, W.Z., 2008. Modeling rainfall conditions for shallow landsliding in Seattle, Washington. Geol. Soc. Am. Rev. Eng. Geol. XX, 137–152.

Griswold, J.P., Iverson, R.M., 2008. Mobility statistics and automated hazard mapping for debris flows and rock avalanches. U.S. Geol. Surv. Sci. Invest. Rep. 2007-5276, 59 p.. http://pubs.usgs.gov/sir/2007/5276/.

Haugerud, R.A., 2014. Preliminary interpretation of pre-2014 landslide deposits in the vicinity of Oso, Washington. U.S. Geol. Surv. Open-File Rep. 2014-1065.

Heim, A., 1882. Der bergsturz von Elm. Z. Dtsch. Geol. Ges. 34, 74–115.

Heim, A., 1932. Bergsturz und Menschenleben (Landslides and Human Lives). Naturforschenden Gesellschaft, Zürich. translated by N.A. Skemer. BiTech Publishers, Vancouver, Canada, 1989.

Hsu, K., 1978. Albert Heim: observations on landslides and relevance to modern interpretations. In: Voight, B. (Ed.), Rockslides and Avalanches. In: Natural Phenomena, vol. 1. Elsevier, Amsterdam, pp. 71–93.

Hungr, O., Evans, S.G., 2004. Entrainment of debris in rock avalanches: an analysis of the long-runout mechanism. Geol. Soc. Am. Bull. 116, 1240–1252.

Hungr, O., Leroueil, S., Picarelli, L., 2014. The Varnes classification of landslide types, an update. Landslides 11, 167–194. http://dx.doi.org/10.1007/s10346-013-0436.

Hutchinson, J.N., Bhandari, R.K., 1971. Undrained loading, a fundamental mechanism of mudflows and other mass movements. Geotechnique 21, 353–358.

Iverson, N.R., Mann, J.E., Iverson, R.M., 2010. Effects of soil aggregates on debris-flow mobilization: results from ring-shear experiments. Eng. Geol. 114, 84–92.

Iverson, R.M., 1997. The physics of debris flows. Rev. Geophys. 35, 245–296.

Iverson, R.M., 2000. Landslide triggering by rain infiltration. Water Res. 36, 1897–1910.

Iverson, R.M., 2005. Regulation of landslide motion by dilatancy and pore-pressure feedback. J. Geophys. Res. 110, F02015. http://dx.doi.org/10.1029/2004JF000268.

Iverson, R.M., Reid, M.E., LaHusen, R.G., 1997. Debris-flow mobilization from landslides. Annu. Rev. Earth Planet. Sci. 25, 85–138.

Iverson, R.M., Schilling, S.P., Vallance, J.W., 1998. Objective delineation of lahar-inundation hazard zones. Geol. Soc. Am. Bull. 110, 972–984.

Iverson, R.M., Reid, M.E., Iverson, N.R., LaHusen, R.G., Logan, M., Mann, J.E., Brien, D.L., 2000. Acute sensitivity of landslide rates to initial soil porosity. Science 290, 513–516.

Iverson, R.M., Logan, M., LaHusen, R.G., Berti, M., 2010. The perfect debris flow? Aggregated results from 28 large-scale experiments. J. Geophys. Res., Earth Surf. 115, F03005. http://dx.doi.org/10.1029/2009JF001514.

Iverson, R.M., Reid, M.E., Logan, M., LaHusen, R.G., Godt, J.W., Griswold, J.G., 2011. Positive feedback and momentum growth during debris-flow entrainment of wet bed sediment. Nat. Geosci. 4, 116–121.

Iverson, R.M., George, D.L., 2014. A depth-averaged debris-flow model that includes the effects of evolving dilatancy: 1. Physical basis. Proc. R. Soc. Lond. Ser. A 470, 20130819. http://dx.doi.org/10.1098/rspa.2013.0819.

Jibson, R.W., 1992. The Mameyes, Puerto Rico, landslide disaster of October 7, 1985. In: Slosson, E., Keene, A.G., Johnson, J.A. (Eds.), Landslides/Landslide Mitigation. In: Geological Society of America Reviews in Engineering Geology, vol. IX, pp. 37–54.

Jibson, R.W., 2006. The 2005 La Conchita, California, landslide. Landslides 3, 73–78. http://dx.doi.org/10.1007/s10346-005-0011-2.

Kanamori, H., Given, J.W., 1982. Analysis of long-period seismic waves excited by the May 18, 1980, eruption of Mount St. Helens – a terrestrial monopole? J. Geophys. Res. 87, 5422–5432.

Legros, F., 2002. The mobility of long-runout landslides. Eng. Geol. 63, 301–331.

Lu, N., Godt, J.W., 2013. Hillslope Hydrology and Stability. Cambridge Univ. Press.

Major, J.J., Pierson, T.C., Scott, K.M., 2005. Debris flows at Mount St. Helens, Washington, USA. In: Jakob, M., Hungr, O. (Eds.), Debris-Flow Hazards and Related Phenomena. Springer, Chichester, pp. 685–731.

Miller, D.J., Sias, J., 1998. Deciphering large landslides: linking hydrological, groundwater and slope stability models through GIS. Hydrol. Process. 12, 923–941.

Mitchell, R.J., Markell, A.R., 1974. Flowsliding in sensitive soils. Can. Geotech. J. 11, 11–31.

Moretti, L., Allstadt, K., Mangeney, A., Capdeville, Y., Stutzmann, E., Bouchut, F., submitted for publication. Numerical modeling of the Mount Meager landslide constrained by its force history derived from seismic data. J. Geophys. Res.

Moriwaki, H., Inokuchi, T., Hattanji, T., Sassa, K., Ochiai, H., Wang, G., 2004. Failure processes in a full-scale landslide experiment using a rainfall simulator. Landslides 4, 277–288.

Ochiai, H., Sammori, T., Okada, Y., 2007. Landslide experiments on artificial and natural slopes. In: Sassa, K., Fukuoka, H., Wang, F., Wang, G. (Eds.), Progress in Landslide Science. Springer, Berlin, Heidelberg, pp. 209–226.

Paguican, E.M.B., van Wyk de Vries, B., Lagmay, A., 2014. Hummocks: how they form and how they evolve in rockslide-debris avalanches. Landslides 11, 67–80. http://dx.doi.org/10.1007/s10346-012-0386-y.

Pailha, M., Pouliquen, O., 2009. A two-phase flow description of the initiation of underwater granular avalanches. J. Fluid Mech. 633, 115–135.

Reid, M.E., Iverson, R.M., Logan, M., LaHusen, R.G., Godt, J.W., Griswold, J.P., 2011. Entrainment of bed sediment by debris flows: results from large-scale experiments. In: Genevois, R., Hamilton, D.L., Prestininzi, A. (Eds.), Fifth International Conference on Debris-Flow Hazards Mitigation, Mechanics, Prediction and Assessment. Casa Editrice Universita La Spienza, Rome, pp. 367–374.

Scheidegger, A., 1973. On the prediction of the reach and velocity of catastrophic landslides. Rock Mech. 5, 231–236.

Schneider, D., Bartelt, P., Caplan-Auerbach, J., Christen, M., Huggel, C., McArdell, B.W., 2010. Insights into rock-ice avalanche dynamics by combined analysis of seismic recordings and a numerical avalanche model. J. Geophys. Res. 115, F04026.

Schofield, A.N., Wroth, C.P., 1968. Critical State Soil Mechanics. McGraw-Hill, New York. 310 p.

Voight, B. (Ed.), 1978. Rockslides and Avalanches. 1. Natural Phenomena. Elsevier, Amsterdam.

Voight, B., Sousa, J., 1994. Lessons from Ontake-san: a comparative analysis of debris avalanche dynamics. Eng. Geol. 38, 261–297.

Voight, B., Janda, R.J., Glicken, H., Douglas, P.M., 1983. Nature and mechanics of the Mount St. Helens rockslide-avalanche of 18 May 1980. Geotechnique 33, 243–273.

Zanchetta, G., Sulpizio, R., Pareschi, M.T., Leoni, F.M., Santacroce, R., 2004. Characteristics of May 5–6, 1998 volcaniclastic debris flows in the Sarno area (Campania, southern Italy): relationships to structural damage and hazard zonation. J. Volcanol. Geotherm. Res. 133, 377–393.